Experimental Results of a 3-D Millimeter-Wave Compressive Reflector Antenna Imaging System

Weite Zhang, Ali Molaei, Juan Heredia-Juesas, Luis Tirado, Katherine Graham, Anthony Bisulco,
Hipolito Gomez-Sousa, and Jose Angel Martinez-Lorenzo

***Abstract*—This letter presents the first experimental results of our three-dimensional (3-D) millimeter-wave compressive reflector antenna (CRA) imaging system. In this prototype, the CRA is 3-D printed and coated with a metallic spray to easily introduce pseudorandom scatterers on the surface of a traditional reflector antenna. The CRA performs a pseudorandom coding of the incident wavefront, thus adding spatial diversity in the imaging region and enabling the effective use of compressive sensing and imaging techniques. The CRA is fed with a multiple-input multiple-output radar, which consists of four transmitting and four receiving ports. Consequently, the mechanical scanning parts and phase shifters, which are necessary in conventional physical or synthetic aperture arrays, are not needed in this system. Experimental results show the effectiveness of the prototype to perform a successful 3-D detection of a T-shaped metallic target.**

***Index Terms*—Compressive reflector antenna (CRA), compressive sensing (CS), millimeter-wave (mm-wave), spatial diversity, 3-D imaging.**

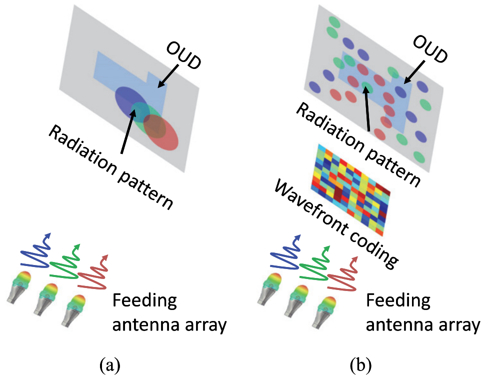

Fig. 1. (a) Conventional imaging system. (b) CS imaging system. OUT: object under detection, which is T-shaped.

I. Introduction

Active microwave and millimeter-wave (mm-wave) systems have been widely used in many applications, such as communications, nondestructive testing, security screening, medical diagnosis, and through-the-wall imaging [1]–[6]. These applications build upon the unique features provided by electromagnetic waves at these frequencies, including, but not limited to, their ability to penetrate through optically opaque materials and their safe use around persons afforded by the nonionizing radiation. Unfortunately, conventional high-resolution mm-wave imaging systems require the use of either expensive physical arrays [7]–[9] or slow synthetic [10], [11] aperture arrays, thus preventing its pervasive usage in societally important applications. Moreover, conventional phased array imaging systems [see Fig. 1(a)] are suboptimal due to the often large mutual information existing between successive measurements [12]. One way to address the aforementioned limitations is to engineer new mm-wave imaging systems capable of making that successive measurements as incoherent as possible; this will enable real-time operation while reducing the number of measurements, hardware complexity, and required energy budget.

Compressive sensing (CS) theory [13], [14] has been widely used to reconstruct signals from undersampled data. CS requires both the unknown signal to be sparse in a given dictionary or basis functions and the sensing matrix—relating the unknown signal and undersampled data—to satisfy the so-called restricted isometric property. In many radar applications, induced sources on the surface of realistic targets can often be approximated by sparse signals [15], thus making a CS framework well suited to be used for imaging in such applications. Under these considerations, the target would be efficiently reconstructed with a small number of measurements.

Introducing artificial structures between the multiple-input multiple-output (MIMO) array and the imaging region can provide an enhanced spatial diversity, as shown in Fig. 1(b), and, as a result of this coding, the number of measurements needed to obtain an acceptable image reconstruction can be reduced even more [16]. Many of these pioneering compressive imaging systems used spatially modulating devices—like dielectric lenses [17], [18] or metasurfaces [19], [20]—to perform such a wavefield-based analog data compression.

Manuscript received July 31, 2018; revised October 9, 2018; accepted October 9, 2018. Date of publication October 11, 2018; date of current version January 3, 2019. This work was supported in part by the National Science Foundation CAREER Program under Award 1653671 and in part by the U.S. Department of Homeland Security under Award 2013-ST-061-ED0001. *(Corresponding author: Jose Angel Martinez-Lorenzo.)*

W. Zhang, A. Molaei, L. Tirado, A. Bisulco, and H. Gomez-Sousa are with the Department of Electrical and Computer Engineering, Northeastern University, Boston, MA 02115 USA (e-mail: zhang.weit@husky.neu.edu; molaei.a@husky.neu.edu; tirado.l@husky.neu.edu; abisulco@gmail.com; hgomez@com.uvigo.es).

J. Heredia-Juesas and J. A. Martinez-Lorenzo are with the Department of Electrical and Computer Engineering and the Department of Mechanical and Industrial Engineering, Northeastern University, Boston, MA 02115 USA (e-mail: j.herediajuesas@northeastern.edu; j.martinez-lorenzo@northeastern.edu).

K. Graham is with the Department of Mechanical and Industrial Engineering, Northeastern University, Boston, MA 02115 USA (e-mail: graham.ka@husky.neu.edu).

Digital Object Identifier 10.1109/LAWP.2018.2875628

This letter presents the first experimental results of our compressive imaging system, which performs the coding using a compressive reflector antenna (CRA) [21], [22]. The CRA is manufactured by coating the surface of a traditional reflector antenna (TRA) with pseudorandom metallic applique scatterers [21]. As a result, the incident wave from the transmitting (Tx) array is spatially coded and, later, reflected toward the region of interest (RoI). The pseudorandom spatial code created by the CRA in the RoI is dynamically changed by selecting different input frequencies and active ports in the MIMO array [23]. The CRA enhances the singular value distribution and sensing capacity of the imaging system when compared to that of the TRA, as we previously showed in [21] and [22], which results in a metric used to quantitatively determine the information transfer efficiency between sensors and RoI [24], thus potentially enabling real-time imaging while reducing the hardware cost and complexity. The rest of this letter is organized as follows. In Section II, the design details of the CRA are described. In Section III, a 3-D mm-wave experimental setup is used to image a T-shaped metallic target, and the 3-D reconstructed images show the reliability of the established cost-effective imaging system, and a conclusion is finally drawn in Section IV.

II. DESIGN AND FABRICATION OF THE CRA-BASED IMAGING SYSTEM

The surface of a TRA, which has its axis of symmetry parallel to the $\hat{y}$-axis, can be mathematically written as follows:

$$y = \frac{(x - L_{\text{off}})^2 + z^2}{4f_0} - f_0$$
$$\{x - L_{\text{off}}, z\} \in [-D_0/2, D_0/2] \tag{1}$$

where D_0 is the aperture size, f_0 is the focal length, and $F = (0, 0, 0)$ is the focal point that is colocated with the phase center of the MIMO array. In order to minimize the blockage of the reflected field from the TRA and to enhance the radiation efficiency, its surface is designed with an offset length of L_{off}, as shown in the left part of Fig. 2(a). The coating of the TRA surface with metallic applique scatterers results in a CRA that performs the spatial coding of the fields reflected from its surface. The metallic applique scatterers can be described by a pseudorandom perturbation function in $\Delta h(x, z)$ in the $\hat{y}$-axis. A geometrical model of the CRA is plotted in the right part of Fig. 2(a), where the support of the $\Delta h(x, z)$ function has been discretized into a tessellated mesh of N_Ω triangular faces. The averaged side length of the triangular facets is d_0, and the distortion for each vertex is drawn from a uniform random distribution $U(-\Delta h_m, +\Delta h_m)$, being Δh_m the maximum allowed distortion. All the parameters of the CRA designed in this work are shown in Table I, where λ_0 is the wavelength corresponding to the center frequency f_c of the radar that is operating with a bandwidth B. The exact distortion heights of all the applique scatterers covering the CRA surface are plotted in Fig. 2(b)—see [21] and [22] for a more in-depth description of CRA's parameters.

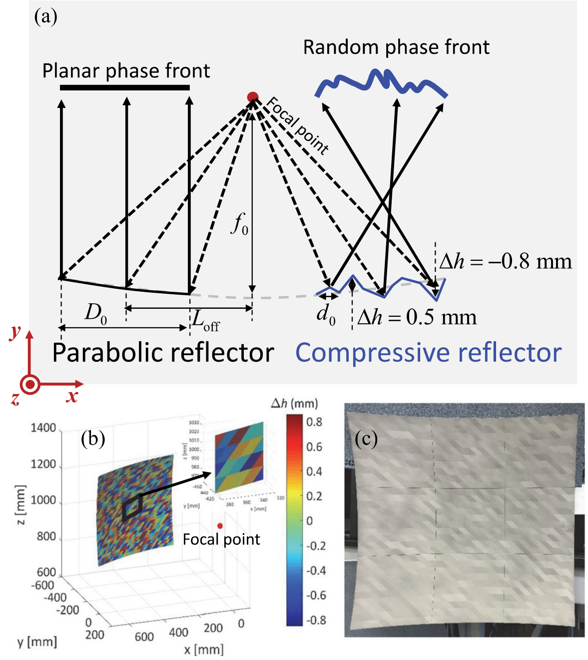

Fig. 2. (a) Off-axis placed parabolic (left) and compressive (right) reflector. (b) Distortion height Δh between the CRA surface and the TRA surface. (c) Fabricated CRA using the 3-D printing technique with its surface covered with metallic triangle units.

TABLE I
PARAMETERS OF THE CRA

Name	Value	Name	Value
D_0	500 mm	Δh_m	0.8 mm
L_{off}	350 mm	λ_0	4.1 mm
f_0	500 mm	B	5 GHz
d_0	16.4 mm	f_c	73.5 GHz

The fabrication of the CRA is done using additive manufacturing techniques. Specifically, an Object Eden 260VS 3-D printer is utilized with VeroWhitePlus as the filament material. Due to limitations on printing size, the CRA is divided into nine parts that are independently printed and assembled together afterwards. The surface of each part is metalized using an acrylic-based silver conductive coating spray. Fig. 2(c) shows the manufactured CRA that is used to perform the wavefield compression and imaging discussed in the next section.

The MIMO array of the CRA uses a frequency-modulated continuous-wave (FMCW) radar front-end (RFE), developed by HXI [25]. The operating frequency range of the RFE is from 70 to 77 GHz; however, only the frequencies from 71 to 76 GHz are used. The radar configuration employs one static Tx and one static receiving (Rx) module. Each module has a single-pole four-throw (SP4T) switch, as shown in the subplot of Fig. 3. The SP4T switches are driven by a field-programmable gate array switching system based on an Altera Cyclone V DE1-SoC board.

III. CALIBRATION OF THE CRA-BASED SENSING MATRIX

Ensuring phase coherence among all Tx and Rx elements of the MIMO array poses an important challenge for this type of

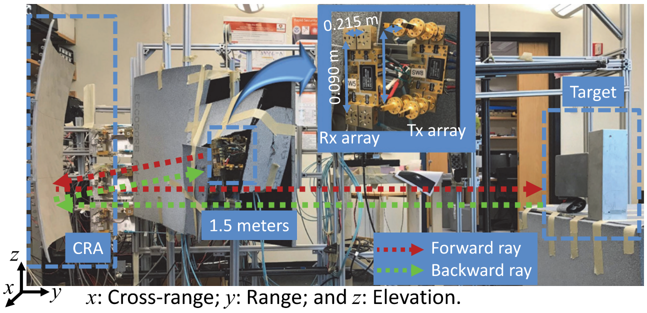

Fig. 3. Experimental setup of the CRA imaging. The forward and backward paths are illustrated in the red and green dashed lines, respectively. A T-shaped metallic target is located 1.5 m away from the center of the CRA. The arrangement and dimensions of the Tx/Rx arrays are shown in the subplot.

high-frequency imaging systems. This is due to the fact that small uncertainties on the relative position of each module—just a fraction of a millimeter—or on the transfer function will hinder the system's ability to perform a successful imaging. In this work, the phase coherence is ensured through a calibration step, in which the field distribution of each array element is measured on an aperture in front of the radar, and these data are later used to build the sensing matrix for one or more RoIs. The field distribution of each array element is collected in a two-step procedure. First, several FMCW chirps are sequentially transmitted from each one of the static MIMO transmitters, and they are measured on the 2-D aperture with a moving receiver. Second, several FMCW chirps are transmitted from a moving transmitter on the same 2-D aperture, and they are measured by each static receiver of the MIMO array.

The recorded fields corresponding to the static Tx and Rx modules are denoted as $\mathbf{E}_{\mathrm{tx}}^{\mathrm{apert}}$ and $\mathbf{E}_{\mathrm{rx}}^{\mathrm{apert}}$, respectively, and they are used to construct a calibrated sensing matrix. First, the equivalent magnetic currents $\mathbf{M}_{\mathrm{tx}}^{\mathrm{aper}}$ and $\mathbf{M}_{\mathrm{rx}}^{\mathrm{aper}}$, corresponding to the transmitters and receivers, respectively, are computed using the equivalence theorem as follows [26]:

$$\mathbf{M}_{\mathrm{tx/rx}}^{\mathrm{apert}} = -2\mathbf{n}_0 \times \mathbf{E}_{\mathrm{tx/rx}}^{\mathrm{apert}} \tag{2}$$

where $\mathbf{n}_0 = [0, 1, 0]$ is the normal vector on the 2-D aperture. Then, the incident fields in the RoI produced by these currents are computed using the exact near-field radiation equations [26] as follows:

$$\mathbf{E}_{\mathrm{tx/rx}}^{\mathrm{RoI}}(\mathbf{r}) = -\frac{1}{4\pi}\int_{S_{\mathrm{apert}}} G_0 \left(\mathbf{M}_{\mathrm{tx/rx}}^{\mathrm{apert}} \times \mathbf{R}\right) e^{-jkR} ds \tag{3}$$

where $G_0 = \frac{1+jkR}{R^3}$; $\mathbf{R} = \mathbf{r} - \mathbf{r}'$, with $\mathbf{r}$ being the point in the RoI and $\mathbf{r}'$ being the point on the 2-D aperture; $R = |\mathbf{R}|$; $k = \frac{2\pi}{\lambda}$ is the wave number; S_{apert} is the surface of the 2-D aperture; and $\mathbf{E}_{\mathrm{tx}}^{\mathrm{RoI}}$ and $\mathbf{E}_{\mathrm{rx}}^{\mathrm{RoI}}$ are the electric fields, generated by $\mathbf{M}_{\mathrm{tx}}^{\mathrm{apert}}$ and $\mathbf{M}_{\mathrm{rx}}^{\mathrm{apert}}$, respectively, in each voxel of the RoI. Finally, the first-order Born approximation [27] can be used to compute the calibrated sensing matrix for each Tx and Rx port $\mathbf{H}_{T,R}$:

$$\mathbf{H}_{T,R} = \mathbf{E}_{\mathrm{tx}}^{\mathrm{RoI}} \cdot \mathbf{E}_{\mathrm{rx}}^{\mathrm{RoI}}. \tag{4}$$

Finally, the concatenation of all sensing matrices for each pair of Tx and Rx ports and for all sampled frequencies gives rise to the full-system sensing matrix $\mathbf{H}$ that will be used for the imaging.

IV. IMAGING ALGORITHM

The imaging algorithm is used to solve the Born-linearized inverse problem: $\mathbf{Hu} + \mathbf{n} = \mathbf{g}$, where $\mathbf{u}$ is the unknown reflectivity vector of the target in the RoI, $\mathbf{g}$ is the measured field scattered by the target, and $\mathbf{n}$ is the noise vector. This problem can be iteratively solved with typical norm-1 regularized algorithms, and in this work, the distributed alternating direction method of multipliers (ADMM) [28] is applied as follows:

$$\begin{aligned} &\text{minimize} \quad \frac{1}{2}\sum_{i=1}^{N} \|\mathbf{H}_i\mathbf{u}_i - \mathbf{g}_i\|_2^2 + \lambda_r \|\mathbf{v}\|_1 \\ &\text{s.t.} \quad \mathbf{u}_i = \mathbf{v}, \forall i = 1, \ldots, N \end{aligned} \tag{5}$$

where the original sensing matrix $\mathbf{H}$ and the measurement vector $\mathbf{g}$ are divided (by rows) into N submatrices $\mathbf{H}_i$ and N subvectors $\mathbf{g}_i$, respectively, $i \in [1, N]$; $\mathbf{u}_i$ is the unknown reflectivity vector for each pair of $\mathbf{H}_i$ and $\mathbf{g}_i$; λ_r is the norm-1 weight factor; and $\mathbf{v}$ is a *consensus* variable that enforces the agreement among all $\mathbf{u}_i$.

In order to mitigate the spatial noise, a 2-D cross-range averaging was applied to the reflectivity function $\mathbf{u}$. The averaging process can be written as follows:

$$\mathbf{u}_a(x_0, y_0, z_0) = \sum_{n_x=-\frac{N_a}{2}}^{\frac{N_a}{2}} \sum_{n_z=-\frac{N_a}{2}}^{\frac{N_a}{2}} \frac{\mathbf{u}(x_0 + n_x, y_0, z_0 + n_z)}{(N_a + 1)^2} \tag{6}$$

where $\mathbf{u}(x_0, y_0, z_0)$ is the reflectivity of the (x_0, z_0)th pixel in the y_0th 2-D plane, and the length of the 2-D averaging process is $N_a + 1$ in each dimension, with N_a being an even number.

V. EXPERIMENTAL RESULTS

The spatial codes created by the fabricated CRA are measured in the near field for the calibration algorithm all throughout the operating bandwidth. Two WR-12 tapered waveguides are used with the moving transmitter and receiver, which are mounted on the scanning platform at 900 mm away from the CRA's center. The fields are collected in an aperture of 880 and 640 mm in the x-axis (cross-range) and the z-axis (elevation), respectively, and sampled every half a wavelength at 77 GHz. The magnitude and phase of the measured fields for one of the MIMO transmitters are plotted for different frequencies in Fig. 4, showing the expected spatially coded patterns.

The experimental setting shown in Fig. 3 is used to image a rotated T-shaped metallic target. In the forward path (illustrated with red dashed line), the four Tx ports of the switch are sequentially used to illuminate the CRA. The incident wavefront is pseudorandomly coded and scattered toward the RoI, where the T-shaped target is placed at its center. In the backward path (illustrated with the green dashed line), the scattered field produced by the target is coded again by the CRA, and the field is scatted toward and measured at all four Rx ports. A total of 30

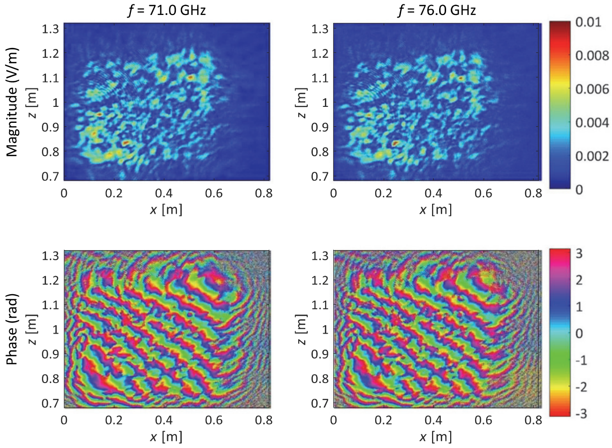

Fig. 4. Measured near-field radiation patterns including the magnitude (top) and phase (bottom) distributions.

evenly spaced frequencies are used in the 5 GHz bandwidth, resulting in a total of 480 measurements (30 frequencies × 4 Txs × 4 Rxs). The dimensions of the RoI are 600, 420, and 600 mm in cross-range, range, and elevation, respectively. The voxel discretization size is selected to be 6, 30, and 6 mm in x-, y-, and z-axis, respectively, which is limited by the upper bound range and cross-range resolution of wideband radar aperture systems [8]:

$$\sigma_{x,z} = \frac{\lambda_0 R}{2D_0}$$
$$\sigma_y = \frac{c}{2B} \tag{7}$$

where $R = 1.5$ m is the range of the target, $D_0 = 500$ mm is the aperture size of the reflector, λ_0 is the free-space wavelength corresponding to the center frequency of 73.5 GHz, c is the speed of light, and $B = 5$ GHz is the operating bandwidth of the radar system. According to the size of the sensing matrix $\mathbf{H} \in R^{M_H \times N_H}$, M_H and N_H being 480 and 153015, respectively, in the experiment, the compression ratio CR $= \frac{N-M}{N} \times 100\% = \frac{153015-480}{153015} = 99.69\%$ is calculated [29].

The norm-1 regularized ADMM algorithm described above is executed—using a weight factor of $\lambda_r = 20$ and dividing the sensing matrix into $N = 40$ blocks. A 5-pixel 2-D averaging processing ($N_a = 4$) is applied afterwards. The selection of the regularization parameters depends on the geometry of the system, as well as computational resources. Specifically, N is limited by the number of available threads of the CPU or GPU, λ_r is the norm-1 weight factor, which should be adjusted according to the received signal-to-noise ratio of the imaging system, and N_a should satisfy $(N_a + 1)\sigma_{x,z}$ [illegible] $\frac{\min\{D_x, D_z\}}{4}$, with D_x and D_y being the minimum size of the target in x- and z- axis, respectively, in order to reduce the spatial noise level while still retaining the original shape of the target. The 3-D reconstruction of the target profile is plotted in Fig. 5. The imaged frame of the reconstructed reflectivity magnitude $|\mathbf{u}|$ at the range $y = 1500$ mm is shown in Fig. 5(a), the maximum magnitude of $|\mathbf{u}|$ along the range (y-axis) is plotted in Fig. 5(b), where the range of the projection domain is 420 mm, and the reconstructed target profile is shown in Fig. 5(c), where a display threshold of $|\mathbf{u}| \geq 0.35$ has been applied. The dimensions of the real T-shaped metallic target are shown in Fig. 5(d). Fig. 5 shows that the CRA-based system is capable of detecting a target in the RoI.

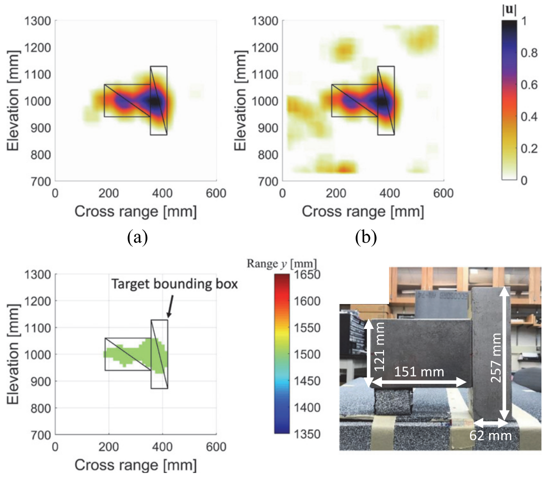

(a) (b)

(c) (d)

Fig. 5. (a) Normalized magnitude of the reconstructed reflectivity, $|\mathbf{u}|$, on the 2-D plane at the range $y = 1500$ mm. (b) Maximum $|\mathbf{u}|$ along the range (y-axis), where the range of the projection domain is 420 mm. (c) Reconstructed target profile with a display threshold of $|\mathbf{u}| \geq 0.35$ and a 2-D averaging length of $N = 5$ pixels. (d) Real T-shaped metallic target under detection. The target bounding box shows the real target profile.

To better evaluate the retrieval accuracy of the reconstructed target reflectivity, an error index is defined as Err $= (1 - \frac{N_{\text{img}}}{N_0}) + \frac{\bar{N}_{\text{img}}}{\bar{N}_0}$, where N_{img} is the number of pixels correctly reconstructed on the surface of the target, $\bar{N}_{\text{img}}$ is the number of pixels incorrectly reconstructed outside the surface of the target, N_0 is the total number of the pixels on the surface of the target, and $\bar{N}_0$ is the total number of the pixels covering the whole RoI but excluding the pixels on the target. Thus, the error index Err $= 31.5\%$ is obtained based on Fig. 5. This error is mainly attributed to the noisy measurements of the sensing matrix $\mathbf{H}$ and the vector $\mathbf{g}$, and the noncoaxial alignment between the target and the CRA.

VI. CONCLUSION

This letter presents the first experimental results of our 3-D mm-wave CRA-based imaging system. The proposed cost-effective imaging system is built using a 3-D-printed CRA fed by a MIMO array that uses four Tx and four Rx ports. The CRA is used to introduce spatial and spectral coding of the wave-fields incident to and scattered from the target, thus enhancing the diversity of successive measurements. Although the proposed system is capable of detecting the target, certain errors still exist in the reconstruction of the targets support and reflectivity function. It is expected that this reconstruction error can be reduced by using additional transmitters and receivers feeding one or multiple CRAs; the latter analysis will be addressed in our future work. This letter paves the way toward developing a new cost-efficient mm-wave imaging system that uses multiple CRAs to image on-the-move human-size targets in security applications.

REFERENCES

[1] I. Kemp, M. Peterson, C. Benton, and D. T. Petkie, “Sub-mm wave imaging techniques for non-destructive aerospace materials evaluation,” *IEEE Trans. Aerosp. Electron. Syst. Mag.*, vol. 25, no. 8, pp. 17–19, Aug. 2010.

[2] S. S. Ahmed, A. Schiessl, F. Gumbmann, M. Tiebout, S. Methfessel, and L. P. Schmidt, “Advanced microwave imaging,” *IEEE Microw. Mag.*, vol. 13, no. 6, pp. 26–43, Sep. 2012.

[3] J. A. Martinez-Lorenzo, F. Quivira, and C. M. Rappaport, “SAR imaging of suicide bombers wearing concealed explosive threats,” *Prog. Electromagn. Res.*, vol. 125, pp. 255–272, 2012.

[4] P. M. Meaney, M. W. Fanning, D. Li, S. P. Poplack, and K. D. Paulsen, “A clinical prototype for active microwave imaging of the breast,” *IEEE Trans. Microw. Theory Techn.*, vol. 48, no. 11, pp. 1841–1853, Nov. 2000.

[5] F. K. Wang, T. S. Horng, K. C. Peng, J. K. Jau, J. Y. Li, and C. C. Chen, “Detection of concealed individuals based on their vital signs by using a see-through-wall imaging system with a self-injection-locked radar,” *IEEE Trans Microw. Theory Techn.*, vol. 61, no. 1, pp. 696–704, Jan. 2013.

[6] J. A. Martínez-Lorenzo, M. Arias, O. Rubiños, J. Gutiérrez, and A. García-Pino, “A shaped and reconfigurable reflector antenna with sectorial beams for LMDS base station,” *IEEE Trans. Antennas Propag.*, vol. 54, no. 4, pp. 1346–1349, Apr. 2006.

[7] J. M. Lopez-Sanchez and J. Fortuny-Guasch, “3-D radar imaging using range migration techniques,” *IEEE Trans. Antennas Propag.*, vol. 48, no. 5, pp. 728–737, May 2000.

[8] D. M. Sheen, D. L. McMakin, and T. E. Hall, “Three-dimensional millimeter-wave imaging for concealed weapon detection,” *IEEE Trans. Microw. Theory Techn.*, vol. 49, no. 9, pp. 1581–1592, Sep. 2001.

[9] B. Gonzalez-Valdes, Y. Alvarez, S. Mantzavinos, C. M. Rappaport, F. Las-Heras, and J. A. Martinez-Lorenzo, “Improving security screening: A comparison of multistatic radar configurations for human body imaging,” *IEEE Antennas Propag. Mag.*, vol. 58, no. 4, pp. 35–47, Aug. 2016.

[10] V. M. Patel, G. R. Easley, D. M. Healy, Jr, and R. Chellappa, “Compressed synthetic aperture radar,” *IEEE J. Sel. Topics Signal Process.*, vol. 4, no. 2, pp. 244–254, Apr. 2010.

[11] J. Yang, J. Thompson, X. Huang, T. Jin, and Z. Zhou, “Random-frequency SAR imaging based on compressed sensing,” *IEEE Trans. Geosci. Remote Sens.*, vol. 51, no. 2, pp. 983–994, Feb. 2013.

[12] D. Bleh *et al.*, “W-band time-domain multiplexing FMCW MIMO radar for far-field 3-D imaging,” *IEEE Trans Microw. Theory Techn.*, vol. 65, no. 9, pp. 3474–3484, Sep. 2017.

[13] D. L. Donoho, “Compressed sensing,” *IEEE Trans. Inf. Theory*, vol. 52, no. 4, pp. 1289–1306, Apr. 2006.

[14] R. Baraniuk and P. Steeghs, “Compressive radar imaging,” in *Proc. IEEE Radar Conf.*, Apr. 2007, pp. 128–133.

[15] M. Rani, S. B. Dhok, and R. B. Deshmukh, “A systematic review of compressive sensing: Concepts, implementations and applications,” *IEEE Access*, vol. 6, pp. 4875–4894, 2018.

[16] Q. Cheng, A. Alomainy, and Y. Hao, “Near-field millimeter-wave phased array imaging with compressive sensing,” *IEEE Access*, vol. 5, pp. 18975–18986, 2017.

[17] S. Popoff, G. Lerosey, R. Carminati, M. Fink, A. Boccara, and S. Gigan, “Measuring the transmission matrix in optics: An approach to the study and control of light propagation in disordered media,” *Phys Rev. Lett.*, vol. 104, 2010, Art. no. 100601.

[18] A. Liutkus *et al.*, “Imaging with nature: Compressive imaging using a multiply scattering medium,” *Sci. Rep.*, vol. 4, 2014, Art. no. 5552.

[19] S. Liu and T. J. Cui, “Flexible controls of scattering clouds using coding metasurfaces,” *Sci. Rep.*, vol. 6, 2016, Art. no. 37545.

[20] J. Gollub *et al.*, “Large metasurface aperture for millimeter wave computational imaging at the human-scale,” *Sci. Rep.*, vol. 7, 2017, Art. no. 42650.

[21] J. A. M. Lorenzo, J. H. Juesas, and W. Blackwell, “A single-transceiver compressive reflector antenna for high-sensing-capacity imaging,” *IEEE Antennas Wireless Propag. Lett.*, vol. 15, pp. 968–971, 2016.

[22] A. Molaei, G. Ghazi, J. Heredia-Juesas, H. Gomez-Sousa, and J. Martinez-Lorenzo, “High capacity imaging using an array of compressive reflector antennas,” in *Proc. 11th Eur. Conf. Antennas Propag.*, Mar. 2017, pp. 1731–1734.

[23] L. Tirado, W. Zhang, A. Bisulco, H. Gomez-Sousa, and J. Martinez-Lorenzo, “Towards three-dimensional millimeter-wave radar imaging of on-the-move targets,” presented at IEEE AP-S Int. Symp., Boston, MA, USA, Jul. 11, 2018.

[24] A. Molaei *et al.*, “Experimental results of a compressive reflector antenna producing spatial coding,” presented at IEEE AP-S Int. Symp., Boston, MA, USA, Jul. 11, 2018, Paper WE-A5.3A.4.

[25] T. Rosa, “HXI model 8300 73 GHz multi-static FMCW radar front end,” Oct. 2012. [Online]. Available: http://dx.doi.org/10.1111/j.1365-2818.1991.tb03168.x

[26] C. A. Balanis, *Advanced Engineering Electromagnetics*, 2nd ed. New York, NY, USA: Wiley, 2012.

[27] L. Poli, G. Oliveri, and A. Massa, “Microwave imaging within the first-order born approximation by means of the contrast-field Bayesian compressive sensing,” *IEEE Trans. Antennas Propag.*, vol. 60, no. 6, pp. 2865–2879, Jun. 2012.

[28] J. Heredia-Juesas, A. Molaei, L. Tirado, W. Blackwell, and J. Martinez-Lorenzo, “Norm-1 regularized consensus-based ADMM for imaging with a compressive antenna,” *IEEE Antennas Wireless Propag. Lett.*, vol. 16, pp. 2362–2365, 2017.

[29] Z. Tian and G. B. Giannakis, “Compressed sensing for wideband cognitive radios,” in *Proc. IEEE Int. Conf. Acoust., Speech, Signal Process.*, Apr. 2007, vol. 4, pp. IV-1357–IV-1360.